

On the Minimum Number of Samples for Sparse Recovery in Spherical Antenna Near-Field Measurements

Bernd Hofmann^{ID}, *Student Member, IEEE*, Ole Neitz^{ID}, *Student Member, IEEE*,
and Thomas F. Eibert^{ID}, *Senior Member, IEEE*

Abstract—A thorough picture is presented on the capability of compressed sensing to reduce the number of measurement samples that are required for a near-field to far-field transformation (NFFFT), based on the spherical vector wave expansion of the radiated field of an antenna under test. To this end, the minimum number of samples for a sparse recovery is determined such that a predefined far-field accuracy can be achieved. As no suitable sampling theorem exists, this is done by performing extensive numerical simulations, considering possible deviations from exact sparsity, the influence of measurement noise, the sampling scheme, and the probe correction. Particularly, the influences are determined not only qualitatively but also quantitatively. The resulting modified phase transition diagrams (PTDs) show that a reconstruction by the quadratically constraint basis pursuit strategy is sufficiently stable and robust for practical purposes. The simulation and measurement results of NFFFTs show that the predictions for the required number of samples hold true. Consequently, the presented approach using modified PTDs allows to reduce the number of measurement samples with predictable accuracy, when the sparsity level is known.

Index Terms—Antenna measurements, compressed sensing (CS), compressive sampling, near-field to far-field transformation (NFFFT), sparse recovery, spherical vector wave expansion.

I. INTRODUCTION

ANTENNA measurements are oftentimes the basis for assessing and improving the performance of antennas. Taking measurements in the near-field (NF) of the antenna under test (AUT) and applying electromagnetic field transformations to obtain the far-field (FF) pattern can save costs and space compared to FF measurements [1]. This particularly applies to electrically large antennas.

The core concept of the near-field-to-far-field transformations (NFFFTs) is to determine a finite set of equivalent sources, representing the AUT such that the measurements by a probe antenna are reproduced. From these sources, the fields radiated by the AUT can be computed anywhere outside the source volume and, hence, also in the FF. Besides surface currents [2]–[4], propagating plane waves [5]–[7] and other

modal expansions [1], the spherical vector wave functions are a well-established basis of the equivalent sources [8], [9]. The fields radiated by the AUT are expressed as an expansion of these bases with the aim to reconstruct the expansion coefficients. To this end, usually a linear system of equations (LSEs) has to be solved.

One major drawback of the field transformation approach, however, is the long measurement time resulting from the large number of sampling points. These are required to achieve a full rank LSE. Often, even more samples are necessary due to the employed NFFFT, for example, in order to achieve a regular spacing for fast Fourier transform based schemes. Consequently, different concepts have been proposed to reduce the number of samples. In [10] and [11], measurements on a coarse grid were interpolated to a finer grid in order to determine additional (virtual) measurements. In [12], the initial number of samples is iteratively increased until the determined FF pattern does not considerably change any more. However, these approaches, as well as the least squares (LS) solution proposed in [13], suffer from a loss in accuracy. Mauermayer and Eibert [14] achieve a reduction in the number of unknowns (and consequently the number of measurements) by considering parts of the AUT with ray optical concepts. This is, however, only suitable for particular AUTs such as reflector antennas.

A theory allowing to reduce the number of measurements for all antennas while keeping the accuracy is compressed sensing (CS). It has its origin in the area of information theory, dealing with the reconstruction of a signal from incomplete frequency information [15]–[17]. It can be interpreted as a new sampling theorem, defining the framework to uniquely solve an underdetermined LSE by incorporating prior knowledge on the structure of the vector of unknowns and the system matrix. More specifically, the expansion coefficients are required to be sparse, that is, only a fraction of the coefficients is allowed to be considerably different from zero. In addition, the matrix of the LSE has to exhibit certain characteristics in order to guarantee that a unique solution exists and CS can determine this solution [18], [19].

In the area of antenna and radar theory, reviews of possible ways to apply CS are given in [20]–[22]. However, concerning antenna measurements, the focus was on array diagnosis from FF observations. In [23], different random sampling strategies

Manuscript received January 8, 2019; revised June 18, 2019; accepted July 8, 2019. Date of publication August 19, 2019; date of current version November 27, 2019. (Corresponding author: Bernd Hofmann.)

The authors are with the Chair of High-Frequency Engineering, Department of Electrical and Computer Engineering, Technical University of Munich, 80290 Munich, Germany (e-mail: bernd.hofmann@tum.de).

Color versions of one or more of the figures in this article are available online at <http://ieeexplore.ieee.org>.

Digital Object Identifier 10.1109/TAP.2019.2935102

0018-926X © 2019 IEEE. Personal use is permitted, but republication/redistribution requires IEEE permission.
See http://www.ieee.org/publications_standards/publications/rights/index.html for more information.

for the more general problem of sampling the electromagnetic field radiated by sparse sources were compared.

A successful application to noisy FF antenna measurements has been reported in [24], where the FF was expanded as a linear combination of spherical harmonics. Indeed, in the context of cosmic microwave background (CMB) radiation, a sparse spherical harmonics recovery with simulation data was already conducted in [25]. However, in both cases, neither the minimal required number of measurements nor the influence of noise or the sparsity (defects) have been investigated. Theoretical bounds concerning the minimum amount of measurements for the spherical harmonics recovery were initially determined in [26] and further improved by introducing different probability measures for the sampling locations in [27]–[29], where the latter was an empirical approach. Still, all these bounds turn out to be overly pessimistic, that is, it can be shown empirically that significantly less measurements suffice.

A first survey of possible challenges arising when applying CS to antenna NF measurements was given in [30], where the considered expansion basis was formed by the spherical vector waves. However, conclusions on the potential of CS in antenna NF measurements could only be conjectured. In [31], a modification of the basis was proposed by shifting the origin of the expansion to the phase center in order to increase the sparsity level. A theoretical investigation of the spherical vector wave expansion was performed in [32] with a similar approach as the one used for the spherical harmonics. More precisely, sparse recovery in a Wigner-D expansion was treated. Again, however, the determined bounds on the number of measurements are overly pessimistic with virtually no hope for improvement (as will be further explained in Section III).

As there are no approaches so far to establish a precise CS undersampling theorem as in [33] for the matrices occurring in the context of a spherical NFFFT, the idea developed in this article is to employ empirical investigations to determine the minimum number of samples for a sparse recovery. More specifically, inspired by the investigations in [34], several phase transition diagrams (PTDs) are determined by simulations, however, in a modified form. They provide the number of measurements depending on the sparsity level and the desired accuracy of the reconstructed FF. Contrary to [34], we investigate also the influences of measurement noise, deviations from exact sparsity, the sampling scheme, and the probe correction. The PTDs can furthermore be interpreted as a characterization of the system matrix of the NFFFT, showing that CS can be applied with predictable accuracy. As recovery strategy, basis pursuit (BP) and its quadratically constrained version are considered. Hence, a thorough picture is given on the capabilities of CS in the area of spherical NFFFTs. Some preliminary results using this approach have already been presented in [35].

This article is organized as follows. Section II introduces the required principles of spherical antenna NF measurements. The applicability of CS to these is assessed in Section III by reviewing the relevant theoretical and practical aspects of CS. In Section IV, the minimum number of measurements is determined that is required for a successful NFFFT with CS. The influence of all relevant factors on this minimum, such

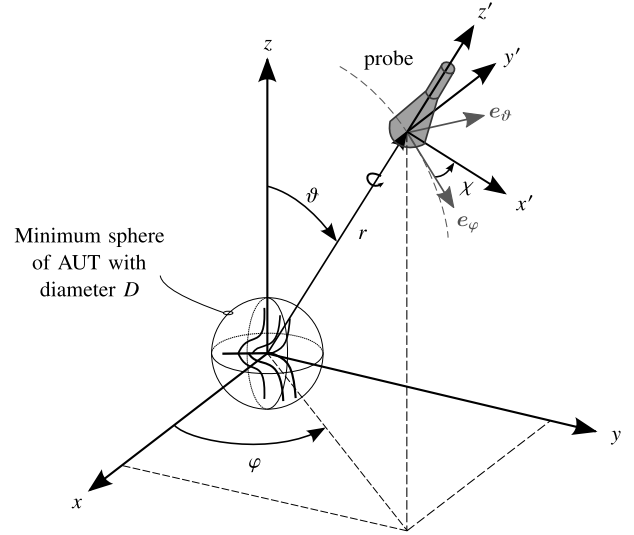


Fig. 1. Considered measurement setup: the probe coordinate system (x', y', z') always points to the origin of the AUT coordinate system (x, y, z) .

as the sampling strategy and the probe correction, is considered qualitatively and quantitatively. The simulation and measurement results of NFFFTs by using CS are presented in Section V, showing that the predictions for the amount of samples for a certain accuracy hold true.

II. SPHERICAL NEAR-FIELD MEASUREMENTS

The considered measurement setup for the spherical NFFFT is shown in Fig. 1. The AUT is placed in the origin of the unprimed (AUT) coordinate system, while the probe antenna and its primed coordinate system are assumed to always point to this origin. The position of the probe with respect to the AUT coordinates is defined by the spherical coordinates $(r^p, \vartheta^p, \varphi^p)$ summarized in the position vector \mathbf{r}^p and the rotation around the z' -axis by the angle χ^p with respect to the unit vector \mathbf{e}_φ .

Assuming the AUT radiates a signal into free space, the fields exterior to the minimum sphere of the AUT can be expressed as a linear combination of the (power normalized) spherical vector wave functions $\mathbf{h}_{smn}^{(4)}$ as defined in [8, p. 13], that is

$$\mathbf{E}_{\text{AUT}}(\mathbf{r}) = \lim_{L \rightarrow \infty} k_w \sqrt{Z_F} \sum_{n=1}^L \sum_{m=-n}^n \sum_{s=1}^2 x_{smn} \mathbf{h}_{smn}^{(4)}(\mathbf{r}) \quad (1)$$

with the expansion coefficients $x_{smn} \in \mathbb{C}\sqrt{W}$ and the summation limit L (commonly referred to as the number of modes) extending to infinity in the general case. The wave impedance of the homogeneous and isotropic background medium is denoted by $Z_F = \sqrt{\mu/\varepsilon}$, where ε is the permittivity and μ the permeability, and k_w is the wavenumber. Furthermore, a harmonic time dependence of $e^{j\omega t}$ is assumed and suppressed, where ω is the angular frequency and j is the imaginary unit with $j^2 = -1$. The FF of the AUT can be obtained by letting $k_w r \rightarrow \infty$, which yields

$$\mathbf{h}_{smn}^{(4)}(r, \vartheta, \varphi) \xrightarrow{k_w r \rightarrow \infty} \frac{e^{-jk_w r}}{k_w r} \mathbf{g}_{smn}(\vartheta, \varphi) \quad (2)$$

with the FF functions $g_{smn}(\vartheta, \varphi)$ as defined in [8, p. 49]. Setting L in (1) to a finite value leads to an acceptable error in the field representation if for an AUT of minimum sphere diameter D , it is chosen as [8, p. 15ff]

$$L \geq \frac{k_w D}{2} + \epsilon \quad (3)$$

where ϵ (should be in the order of 10) is introduced empirically to increase the accuracy (see [8, p. 20ff] for the impact).

The signal y received by the probe antenna can be related to the expansion coefficients by (the transmission formula)

$$y(\mathbf{r}^p, \chi^p) = \sum_{n=1}^L \sum_{m=-n}^n \sum_{s=1}^2 x_{smn} A_{smn}(\mathbf{r}^p, \chi^p) \quad (4)$$

where the influence of the probe and its position is captured in the coefficients

$$A_{smn}(\mathbf{r}^p, \chi^p) = \frac{1}{2} \sum_{\mu=-n}^n \sum_{\sigma=1}^2 \sum_{\substack{\nu=|\mu| \\ \nu \neq 0}}^{\infty} D_{\mu nm}(\vartheta^p, \varphi^p, \chi^p) \times C_{\sigma \mu \nu sn}(k_w r^p) R_{\sigma \mu \nu}^p. \quad (5)$$

Here, $D_{\mu nm} = e^{-jm\varphi^p} d_{\mu nm}(\vartheta^p) e^{-j\mu\chi^p}$ are the Wigner-D functions with $d_{\mu nm}$ as defined in [8, p. 343ff] and $C_{\sigma \mu \nu sn}$ constituting translation functions as defined in [8, p. 355ff]. The coefficients $R_{\sigma \mu \nu}^p$ capture the receiving characteristic of the probe antenna based on the multimode scattering matrix description derived in [8, p. 27ff]. Moreover, for (4) to be valid, multiple reflections between probe and AUT should be negligible.

The summations in (4) can be expressed in vector notation with an arbitrary ordering of the coefficients. Collecting M measurements and stacking the received signals y into the measurement vector $\mathbf{y} \in \mathbb{C}^M$, sorting the corresponding A_{smn} into the sensing matrix $\mathbf{A} \in \mathbb{C}^{M \times N}$, and calling the vector with the expansion coefficients $\mathbf{x} \in \mathbb{C}^N$, the LSE

$$\mathbf{y} = \mathbf{A}\mathbf{x} \quad (6)$$

can be formulated. The number of coefficients can be determined as $N = 2L(L+2)$. Solving (6) for \mathbf{x} allows one to compute the field of the AUT by evaluating (1) or alternatively the FF by using the limit given in (2). A full-rank LSE leading to a unique solution of (6) can be obtained by taking $M = N$ measurement samples. However, often more samples are taken in order to average out noise. Furthermore, and contrary to the proposed approach, often two orthogonal polarizations are measured at each point.

III. APPLICABILITY OF COMPRESSED SENSING

As mentioned in Section I, CS allows one to uniquely solve the LSE in (6) for $M \leq N$, that is, although the LSE is underdetermined. Requirement for this unique solution is that \mathbf{x} is sparse or compressible.

A. Sparsity and Compressibility

The vector \mathbf{x} is referred to as k -sparse, if at most k of its entries are different from zero. More formally, $\|\mathbf{x}\|_0 := \text{card}(\text{supp}(\mathbf{x})) \leq k$ has to hold, with $\text{supp}(\mathbf{x}) = \{i \in \{1, 2, \dots, N\} \mid x_i \neq 0\}$ denoting the support of \mathbf{x} and $\text{card}(\mathcal{S})$ denoting the cardinality of a set \mathcal{S} .

Since real-world signals, represented by the vector \mathbf{x} , are rarely exactly k -sparse, a relaxation to compressible signals can be considered. A common approach is to approximate \mathbf{x} by a k -sparse vector $\hat{\mathbf{x}}$ such that the introduced ℓ_p error σ_k is minimized, that is, $\sigma_k(\mathbf{x})_p = \min_{\hat{\mathbf{x}} \in \mathcal{S}_k} \|\mathbf{x} - \hat{\mathbf{x}}\|_p$, where $\mathcal{S}_k = \{\mathbf{x} \in \mathbb{C}^N \mid \|\mathbf{x}\|_0 \leq k\}$ defines the set of all k -sparse vectors (see [36, p. 42]). Without further specification, the signal is then called compressible, if σ_k decays quickly with increasing k . However, in this article, a more practical measure for the level of sparsity defects is introduced. With

$$\tau = \frac{\max_{smn} |x_{\text{defect}}|}{\max_{smn} |x_{smn}|} \quad (7)$$

the ratio of the maximum magnitude of a coefficient x_{defect} considered as defective (i.e., close to but not exactly zero) to the maximum of all coefficients x_{smn} is measured. This definition will be used in Section IV to investigate the influence of deviations from exact sparsity.

B. Recovery Strategy

For the actual recovery of a k -sparse vector \mathbf{x} , different approaches (see [37] for an overview) have been proved to give the exact solution to the underdetermined LSE (under additional conditions outlined in Section III-C). The strategy considered in this article is to solve the optimization problem

$$\hat{\mathbf{x}} = \arg \min_{\mathbf{z} \in \mathbb{C}^N} \|\mathbf{z}\|_1 \quad \text{s.t.} \quad \mathbf{y} = \mathbf{A}\mathbf{z} \quad (8)$$

which is called BP. For the case that the measurements are contaminated with noise, such that (6) becomes $\mathbf{y} = \mathbf{A}\mathbf{x} + \mathbf{e}$, it might be advantageous to generalize the minimization in (8) to

$$\hat{\mathbf{x}} = \arg \min_{\mathbf{z} \in \mathbb{C}^N} \|\mathbf{z}\|_1 \quad \text{s.t.} \quad \|\mathbf{A}\mathbf{z} - \mathbf{y}\|_2 \leq \eta \quad (9)$$

what is referred to as quadratically constrained BP and abbreviated in this article as BP $_{\eta}$. The choice of the parameter η depends on the noise level (e.g., for bounded noise $\|\mathbf{e}\|_2 \leq \eta$) and will be addressed in more detail in Section IV. Note that the strategies (8) and (9) were also the ones considered in [24]–[32]. While other approaches like greedy- or thresholding-based methods [37] can be less computationally demanding (see [36, p. 73] for a discussion), BP and BP $_{\eta}$ usually require less measurements for a successful recovery [38, p. 358f].

C. The Required Number of Measurements

The most intricate aspect of CS is to determine recovery guarantees stating an exact number of measurements required for successful recovery. Ideally, for the underdetermined LSE in (6) and a specific recovery algorithm, a sampling theorem

would give the exact minimum M as a function of k , N , and \mathbf{A} for a known sparsity k , that is, $M > f(k, N, \mathbf{A})$. Preferably, also noise and sparsity defects are considered. With the intention to do so, different approaches either classify the matrix \mathbf{A} or capture its relevant properties in a characteristic value.

1) *Null Space Property, Coherence, and RIP*: The first recovery guarantee for an arbitrary sensing matrix was given by characterizing its null space. This characterization is, however, non-deterministic polynomial-time hard (NP-hard) to compute and, therefore, not relevant for practical purposes [38, p. 24]. In contrast, the coherence of a matrix (see [39], [40]) is feasible to compute but leads (necessarily) to guarantees in the form of $M \geq C k^2$ with a universal constant C [36, p. 125]. Due to the contained quadratic dependence, this approach is only suited for very sparse vectors \mathbf{x} , which cannot be expected for general antennas.

The probably most dominant tool used to determine recovery guarantees in CS is the restricted isometry property (RIP) originally introduced in [41]. Despite the attention the RIP experienced, it has two major drawbacks making it uninteresting for antenna NF measurements (and other practical purposes). Like the null space property, it is NP-hard to compute [42]. As a workaround, only random matrices (e.g., Bernoulli, Gaussian, and sub-Gaussian distributed) have been considered [18]. For these, it can be shown that the RIP holds with high probability. The second drawback is that even if the RIP constant can be determined, the lower bounds on the minimal number of required measurements are overly pessimistic. According to [33], the most precise bound in terms of the RIP has been given by [43]. Still, it can be shown by numerical experiments that far fewer measurements suffice for a reliable recovery [34]. This can partially be explained by the fact that the RIP is only a sufficient condition for the BP to be successful [38, p. 310].

2) *Bounded Orthonormal Systems*: The only recovery guarantee given so far for antenna NF measurements is based on associating the sensing matrix to a bounded orthonormal system (BOS) [32]. This means that the entries of the sensing matrix are linked to a set of orthonormal functions $\{\phi_1, \dots, \phi_N\}$ which are uniformly bounded with some constant B as $\|\phi\|_\infty \leq B$ in the form of $(\mathbf{A})_{lq} = \phi_q(\mathbf{t}_l)$, where \mathbf{t}_l are the sampling points distributed according to a probability measure (see [44, p. 19ff]). Since for the Wigner-D functions $D_{\mu\nu m}$ in (5) such a uniform bound can be found, this approach seems to be appropriate. However, the derived recovery guarantees are linked to the RIP and consequently overly pessimistic with virtually no hope for significant improvement [33].

3) *Precise Undersampling Theorems*: Due to the empirical observation of a phenomenon called phase transition in [45] and [46], new approaches have arisen. According to this phenomenon, if for a certain number of measurements the sparsity is below a certain threshold, the BP strategy will recover \mathbf{x} with overwhelming probability, above the threshold the recovery fails with high probability. Theoretically, the phase transition was explained in [45]–[47], summarized in [33].

Key feature of the projected polytope approach is that it gives a necessary and sufficient condition for successful recovery and consequently establishes a precise undersampling theorem. While the analysis is asymptotic in the first place (i.e., $N \rightarrow \infty$), it is shown in [48] that for finite N , the number of samples has to be increased with decreasing N . Drawbacks are that the approach is limited to the real-valued case and more importantly to Gaussian random matrices. The same limitations hold for the nullspace Grassmann angle approach proposed in [49], which, however, indicates that (as put in [33]) no “qualitative gap” occurs between the exact sparse case and compressible signals. With increasing deviations from exact sparsity, the number of measurements have to be increased continuously for a recovery.

4) *Observed Universality*: Since in the considered field transformation, the sensing matrix is complex valued and has no random Gaussian distribution, none of the available precise undersampling theorems is fitting. (Note that there are also other but less sharp approaches aiming at a precise undersampling theorem, such as [50]–[53].) Even though they provide some insights, the perhaps most promising results are the ones obtained by extensive numerical simulations in [34]. The idea was to determine the phase transition of different kinds of (random) matrices by simulating several combinations of sparsity k and number of samples M . The simulations reveal that all considered matrices exhibit the same phase transition. Furthermore, the results show that the asymptotic theory works accurately already at moderate N . This leads Donoho and Tanner [34] to the hypothesis that there has to be a larger class of matrices, which all obey the Gaussian phase transition. Although, up to now this class has not been identified, the results suggest that sparse recovery with a moderate amount of samples M is possible for a large variety of sensing matrices.

5) *Uniform and Nonuniform Recovery*: An important distinction made by the above approaches is between strong (uniform) and weak (nonuniform) recovery guarantees [36, p. 48ff]. In terms of antenna measurements, the strong one can be interpreted as choosing the sampling points once at random (determining the sensing matrix) and using them for all AUTs. The weak guarantee corresponds to choosing the sampling points at random for each AUT anew. In the latter case, considerably less measurements should be required to guarantee a successful recovery. A possible interpretation of this circumstance is that the probability that one distribution of sampling points is suitable for all AUTs is much smaller than the probability that a set of (random) points fits for only one AUT. However, as it turns out in Section IV, even for a deterministic set of sampling points, recovery guarantees very close to the weak ones can be achieved.

IV. MINIMUM NUMBER OF SAMPLES FOR CS IN THE SPHERICAL NFFFT

Despite the lack of CS theories fully fitting to antenna measurements, their insights reveal that useful recovery guarantees can also be achieved for the matrices employed in antenna NF measurements. Therefore, it is proposed to determine the minimum number of samples by simulations yielding PTDs.

Beyond that, and for the first time, the impact of all potential influence factors is quantified with the PTDs.

A. Setting up the PTDs

The general concept of PTDs is to perform several reconstructions for all possible combinations of sparsity k and the number of measurements M for a certain sensing matrix \mathbf{A} and to record the percentage of success. To this end, the vector \mathbf{x} of size N is generated by setting k random entries (chosen uniformly at random) of \mathbf{x} to random complex numbers drawn from the standard normal distribution, all other entries are zero. After the selection of the sampling locations r^p and the probe orientation angles χ^p , the sensing matrix is constructed following (5) with an implementation following the approach described in [9]. The number of modes is fixed to $L = 8$ resulting in $N = 160$ coefficients. While this would be a very small number of modes for actual antennas, it can be assumed that the results also hold for any larger L . This assumption is based on the results of [48] (for increasing N , the results hold even better) and verified in Section IV-E. For the values of $M = 16, 48, 80, 112, 144$, and 160 , the sparsity k is varied and for each combination (M, k) , $R = 150$ problem instances are considered. Usually, the sparsity is varied from 1 to M . However, in order to reduce the computation time, k is only increased until the percentage of success drops below 1%. The remaining values for k are not simulated, since it can be expected that all reconstructions in this parameter regime are not successful. Furthermore, at each M , the last k is recorded for which the recovery success is 100%. This is then the first k to be simulated for the next M . Hence, only the area around the phase transition is simulated. For each problem instance, the BP or its quadratically constrained version BP_η is solved. To this end, the CVX MATLAB package is used [54], [55] together with the solver from MOSEK [56]. (Note that a fast solution of the BP or the BP_η problem can be achieved by using, for example, the solution approach described in [57]. This approach does not require the sensing matrix explicitly but only products of the form \mathbf{Ax} (see also [9]).) A success for the reconstructed solution is recorded if the maximum occurring reconstruction error \aleph is below a certain threshold.

To verify that a phase transition occurs at all, the sampling points are initially distributed uniformly at random over the surface of a sphere with radius $r^p = 5$ m (i.e., $\varphi = 2\pi u$ and $\vartheta = \arccos(2v - 1)$ with u and v chosen randomly from $[0, 1]$) and the polarization angles χ^p are selected uniformly at random from the interval $[0, \pi/2]$. (The sampling locations are generated for each reconstruction anew, i.e., a weak transition bound is simulated). A Hertzian dipole (HD) is used as probe antenna. The determined PTD is depicted in Fig. 2. The number of measurements M and the sparsity k are related to the number N of entries in \mathbf{x} by $\delta = M/N$ and $\zeta = k/N$. The domain $(\delta, \zeta) \in [0, 1]^2$ is called phase space. For a successful recovery by the BP strategy $\|\mathbf{x} - \hat{\mathbf{x}}\|_\infty \leq 10^{-6}$ is demanded. The colors indicate the percentage of success, from yellow 0% to blue 100%. The parameters in the white areas were not simulated. With the occurring steep change from 100% to 0%, a phase transition can be identified.

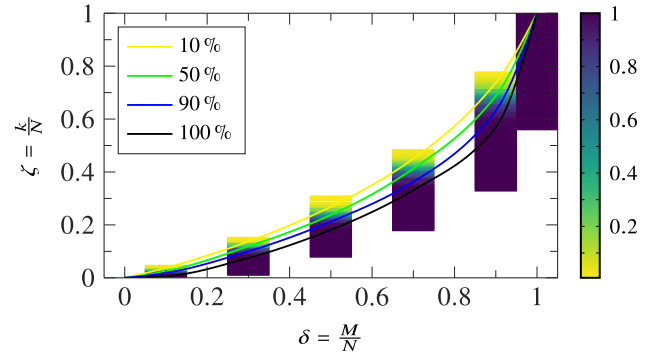


Fig. 2. PTD: sampling points are distributed uniformly at random over the surface of a sphere with radius $r^p = 5$ m. The polarization angles are selected uniformly at random from the interval $[0, \pi/2]$. For a successful recovery by the BP, $\|\mathbf{x} - \hat{\mathbf{x}}\|_\infty \leq 10^{-6}$ is demanded. The depicted lines are in ascending order from top to bottom from 10% to 100%.

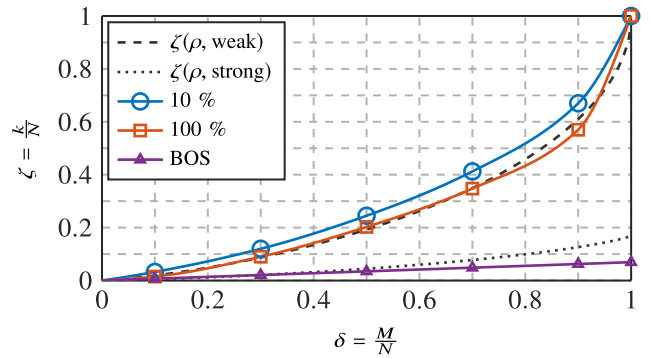


Fig. 3. Extracted success curves of 10% and 100% from the PTD in Fig. 2. The BOS bound corresponds to (10) with the constant C chosen such that the bound is in all points not larger than the empirical 100% curve.

B. Comparison With Theoretical Bounds

For a better comparison also with other bounds, the largest k are extracted for which 10% and 100% recovery success is achieved. The corresponding curves together with the theoretical bounds from the BOSs and the projected polytope approach are depicted in Fig. 3. For interim values, a cubic interpolation is performed (the markers highlight the actually simulated points). It can be seen that not only a phase transition is occurring, but it is also close to the theoretical bound $\zeta(\rho, \text{weak})$ known from the projected polytope approach. This is quite notable, as the sensing matrix is not a random Gaussian matrix (but has considerable structure), $N = 160$ is of moderate size and the setting (sensing matrix, expansion coefficients and measurements) is complex valued. (Note that the numerical computation of $\zeta(\rho, \text{weak})$ and $\zeta(\rho, \text{strong})$ is described in [48] and tabulated values are provided in MATLAB format in [58].) Furthermore, the empirical bounds excel the prediction of the theoretical curve $\zeta(\rho, \text{weak})$ for $M = N$. Consequently, a reconstruction in antenna NF measurements can be even successful for all levels of sparsity (i.e., also for $k = N$). The curve for the BOS method was determined according to the result of [32], requiring

$$M \geq C N^{1/6} k \log^3(k) \log(N) \quad (10)$$

where the universal constant C was chosen such that the bound is in all points not larger than the empirical 100% curve

(since no explicit values are available for C). Also, note that while the bound given in [32] was classified as strong, the same bound is achieved for weak recovery. This is due to the same functional dependence on k in the theorems for strong (see [44, p. 26ff]) and weak (see [36, p. 393]) recovery, whereas all other dependencies are compensated by the universal constant. Compared to the (weak) empirical 100% bound, the BOS bound is far from being optimal.

C. The Error Definition

Before investigating different influences on the reconstruction performance, the question arises how to properly define the reconstruction error for antenna NF measurements. Certainly, the so far used requirement $\|\mathbf{x} - \hat{\mathbf{x}}\|_\infty \leq 10^{-6}$ for a successful recovery is too restrictive when noise is included. The theorems for robust recovery suggest to consider errors of the form $\|\mathbf{x} - \hat{\mathbf{x}}\|_p \leq C\eta$ for bounded noise $\|\mathbf{e}\|_2 \leq \eta$. For the spherical harmonics recovery in [24], the mean squared error $\text{MSE}(\hat{\mathbf{x}}) = \mathcal{E}[(\mathbf{x} - \hat{\mathbf{x}})^2]$ was put forward with \mathcal{E} denoting the expected value. However, it is difficult to impose requirements on the error of the reconstructed coefficient vector (e.g., require that $\|\text{MSE}(\hat{\mathbf{x}})\|_\infty$ is smaller than some bound). In antenna measurements, the quantity of interest is usually the FF pattern, for which requirements on the accuracy are defined. A common (logarithmic) definition of a relative error \aleph is

$$\aleph = \max_{\vartheta, \varphi} \left\{ 20 \log \frac{|E^{\text{FF}}(\vartheta, \varphi) - \hat{E}^{\text{FF}}(\vartheta, \varphi)|}{\max_{\vartheta, \varphi} |E^{\text{FF}}(\vartheta, \varphi)|} \right\} \quad (11)$$

which is then required to stay below a certain level (e.g., $\aleph \leq -60$ dB). Here, E^{FF} and \hat{E}^{FF} denote the magnitude of the reference and the reconstructed FF, respectively. In order to transfer such a definition to the coefficient vectors \mathbf{x} and, $\hat{\mathbf{x}}$ a kind of propagation of error would be necessary based on the relationship in (1) together with (2). However, since no recovery guarantees of the form $\|\mathbf{x} - \hat{\mathbf{x}}\|_p \leq C\eta$ are at hand, it seems more natural to just evaluate the error in the FF pattern. To this end, $E^{\text{FF}}(\vartheta, \varphi)$ and $\hat{E}^{\text{FF}}(\vartheta, \varphi)$ are determined from \mathbf{x} and $\hat{\mathbf{x}}$ on a grid with a resolution of approximately 5.6° in ϑ and φ (32 values in ϑ and 64 values in φ) and the worst case error (11) is determined.

Having defined the error \aleph , it is useful to introduce a modified PTD as the one shown in Fig. 4. Instead of the success rate (for a certain required error), the average of the R reconstruction errors \aleph for the combinations (k, M) is depicted. In this way, the required number of measurements can be determined for a certain sparsity and a desired error from the diagram. In the following, mostly extracted transition bounds from such PTDs are used for comparisons. The choice of $\aleph \leq -60$ dB for the noiseless case is somewhat arbitrary but is in a practical range and well suited for the comparisons. As can be seen from Fig. 4, far smaller errors can be achieved.

D. Influence of the Sampling Grids

As a next step, the influence of different sampling grids is investigated. The corresponding transition bounds are depicted

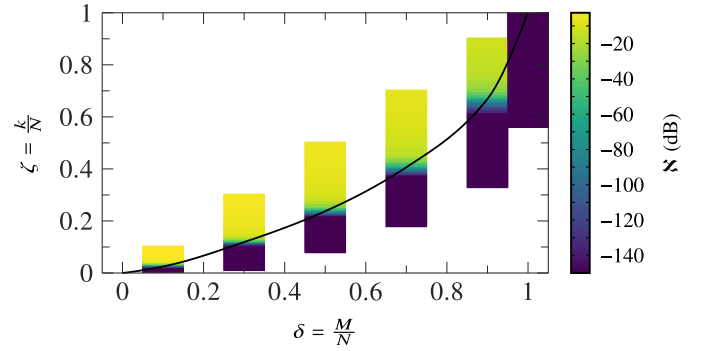


Fig. 4. PTD not showing the success rate but the average reconstruction error \aleph (in dB) for different combinations of (k, M) . In order to increase the resolution for lower accuracies, all error levels smaller than -150 dB were set to -150 dB. The depicted transition bound corresponds to the largest k for which $\aleph \leq -60$ dB is achieved.

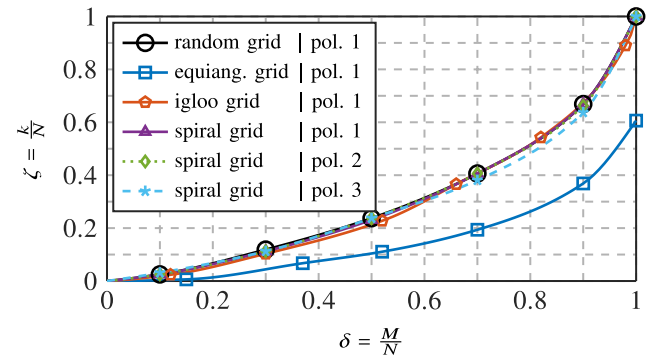


Fig. 5. Transition bounds corresponding to $\aleph \leq -60$ dB for different sampling grids using the BP as recovery strategy. The polarization (pol.) angles χ were chosen according to pol. 1: each selected uniformly at random from the interval $[0, \pi/2]$; pol. 2: each selected uniformly at random from $\{0, \pi/2\}$; and pol. 3: for consecutive points, the polarization is alternately 0 and $\pi/2$.

in Fig. 5 (still for an HD as probe antenna). Again for interim values between the markers, cubic interpolation is used. Firstly, grids are compared where the polarization angles were selected uniformly at random from the interval $[0, \pi/2]$ (pol. 1). As can be expected (from the classical PTD in Fig. 3), distributing the M sampling points uniformly at random over the surface of a sphere yields a useful transition bound. In contrast, when using an equiangular grid, the bound shifts downward considerably. It might be conjectured that, when using so few samples, it is detrimental to have areas where the sampling locations are concentrated more densely. This is also confirmed by the “igloo” distribution introduced in [24] with a spacing of $\Delta\varphi = \Delta\vartheta / \sin\vartheta$ and $\Delta\vartheta = \text{const}$. The scheme reduces the density at the poles but does not achieve a uniform distribution. Consequently, the bound is closer to the one with random sampling but still slightly worse. Almost identical to the random sampling is the bound of a spiral grid which is designed to approximate a uniform distribution of the sample points over the sphere. In particular, the used spiral grid is the one presented in [59]. Introducing the auxiliary parameters

$$h_m = -1 + \frac{2(m-1)}{M-1} \quad (12)$$

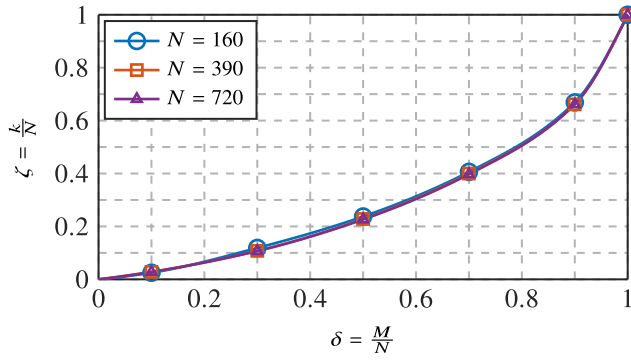


Fig. 6. Transition bounds corresponding to $\aleph \leq -60$ dB for different number of expansion coefficients N using the BP recovery strategy.

for $1 \leq m \leq M$, the measurement positions are computed as

$$\vartheta_m = \arccos(h_m) \quad (13)$$

and

$$\varphi_m = \left(\varphi_{m-1} + \frac{3.6}{\sqrt{M}} \frac{1}{\sqrt{1-h_m^2}} \right) \bmod 2\pi \quad (14)$$

for $2 \leq m \leq M-1$, where $\varphi_1 = \varphi_M = 0$. Since the spiral grid is better suited for measurements than a random grid, it is used for all further investigations. While there are other grids which could work well with CS, each has to be checked individually with the proposed approach.

Concerning the selection process of the polarization angles, two more options are considered. When the χ^p are randomly chosen to be either 0 or $\pi/2$, the transition bound is virtually the same as for polarization 1. Finally, if for consecutive points the polarization is alternately 0 and $\pi/2$, the transition bound slightly shifts down. However, the bound is still in a useful range despite no more randomness is involved in the measurement process. This is quite notable, since the predictions of strong transition bounds (to which it now has to be compared) are usually considerably more pessimistic.

E. Influence of the Problem Size

Using the spiral grid with pol. 1, it is verified in Fig. 6 that the number of expansion coefficients N can be increased without having influence on the transition bound. Consequently, the determined bounds are also valid for large antennas.

F. Influence of Sparsity Defects—Stability

In order to investigate the stability, that is, the influence of deviations from exact sparsity, sparsity defects are added to the coefficient vector \mathbf{x} . More precisely, scaled Gaussian noise such that the maximum value is equal to $\tau \max_{smn} |x_{smn}|$ is added to the vector \mathbf{x} [see (7) for the definition of τ]. However, it is added only to the $N-k$ coefficients which are initially zero. The resulting coefficients in \mathbf{x} are the ones to be reconstructed and based on them, the measurement samples are created ($\mathbf{y} \leftarrow \mathbf{Ax}$).

The resulting transition bounds for different τ -values and the reconstruction approach BP are shown in Fig. 7. In general,

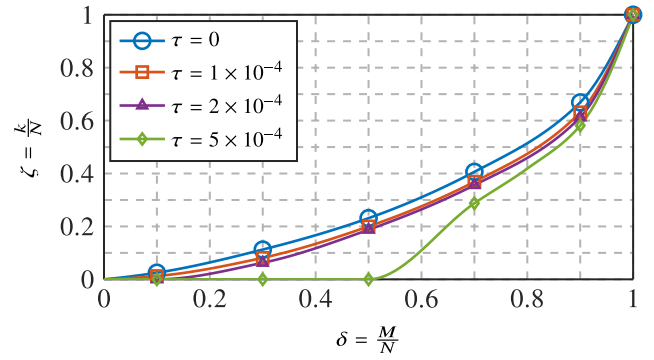


Fig. 7. Transition bounds corresponding to $\aleph \leq -60$ dB for different levels of sparsity defects τ using the BP recovery strategy.

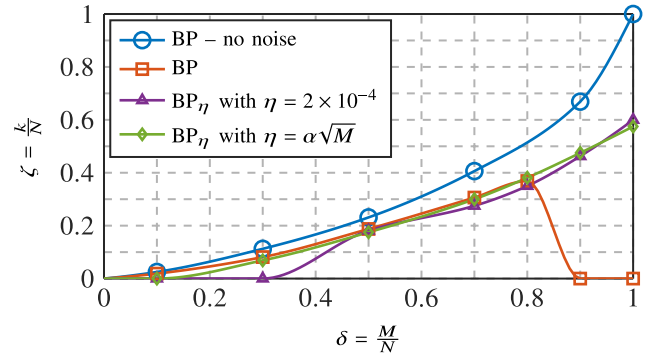


Fig. 8. Transition bounds corresponding to $\aleph \leq -45$ dB for an SNR of 60 dB and different recovery strategies, where $\alpha = 1.975 \times 10^{-5}$. The transition bound for the noiseless case is depicted as well.

with increasing τ , the transition bound is shifted downward. For $M = N$, all sparsity levels can always be reconstructed, which is evident from the fact that at most N coefficients can be different from zero and consequently, there is no difference for different τ -levels at $\delta = 1$. Important is that (as put in [33]) no “qualitative gap” occurs between the exact sparse case ($\tau = 0$) and compressible signals. The transition bounds shift downward continuously. However, and contrary to [49], the approach presented here can quantify the shift. Note that the chosen values for τ appear to be in a practical range considering the expansion coefficients of different antennas (see also Section V).

G. Influence of Noise—Robustness

Besides the stability against sparsity defects, also the robustness against measurement noise is of interest. In order to examine such an influence, complex white Gaussian noise is added to the measurement vector in the form of $\mathbf{y} = \mathbf{Ax} + \mathbf{e}$. A certain signal-to-noise ratio (SNR) is achieved by measuring the maximum power of the signal $P_{\text{sig}} = \max |y_i|^2$ and scaling the noise level such that $\max |\mathbf{e}_i| = \sqrt{P_{\text{sig}}/SNR}$.

As can be seen in Fig. 8 for an SNR of 60 dB, when the BP strategy is used, the bound in general shifts downward compared to the noiseless case. While reconstruction errors of $\aleph \leq -55$ dB are still achievable, the bounds for $\aleph \leq -45$ dB are depicted since otherwise the transition bounds shift downward quite far. However, from a practical perspective, an error

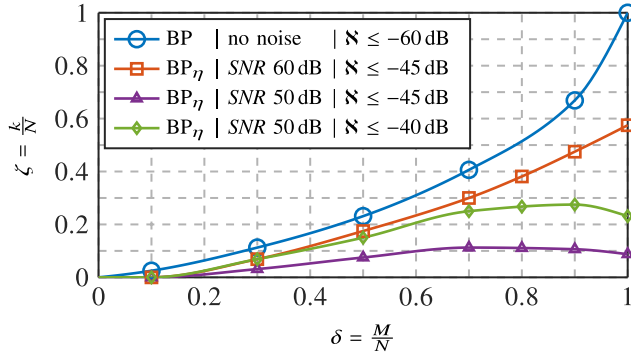


Fig. 9. Transition bounds for different noise levels and the recovery strategy BP_η , where η was chosen as $\eta = \alpha\sqrt{M}$ with $\alpha = 1.975 \times 10^{-5}$ for an SNR of 60 dB and $\alpha = 2.175 \times 10^{-5}$ for an SNR of 50 dB.

of $N \leq -45$ dB is still in a useful range. For $\delta \gtrsim 0.8$, the allowed sparsity level for a successful reconstruction even decreases when the number of measurements is increased. A possible explanation for this decrease could be that the BP assumes all measurements to be exact due to the side condition in (8). Consequently, when more (noisy) measurements are added, more defective information is also added.

As a remedy, the quadratically constrained version of the BP, BP_η [see (9)] is used. For a fixed (empirically determined) $\eta = 2 \times 10^{-4}$, the transition bound also increases for $\delta \gtrsim 0.8$ but is otherwise worse than the BP bound. The right choice of η is crucial, as is also shown theoretically in [60]. However, since the measurement noise is not bounded by a fixed η (i.e., $\|\mathbf{e}\|_2 \leq \eta$) but rather Gaussian distributed, there is no ultimate choice. One approach could be to leverage a tail bound which states that $\exists c > 0$ such that for any $\epsilon > 0$

$$\mathcal{P}(\|\mathbf{e}\|_2 \leq (1 + \epsilon)\sigma\sqrt{M}) \geq 1 - e^{-c\epsilon^2 M} \quad (15)$$

where $\mathcal{P}(\mathcal{E})$ denotes the probability of the event \mathcal{E} and σ is the variance [38, p. 32]. Consequently, the parameter should be chosen depending on the number of measurements as $\eta = \alpha\sqrt{M}$, where α has to be increased with an increasing noise level. This is also verified numerically by the improved bound (compared to $\eta = 2 \times 10^{-4}$) shown in Fig. 8. Note, however, that the empirically chosen $\alpha = 1.975 \times 10^{-5}$ might not be optimal yet.

Using the approach with $\eta = \alpha\sqrt{M}$, transition bounds for different noise levels are determined. The results are depicted in Fig. 9. They show that the bound shifts downward with decreasing SNR . While the bound for an SNR of 50 dB shifts down considerably, a relaxation of the requirement for the error to $N \leq -40$ dB (also depicted in Fig. 9) suffices to shift the transition bound back to a useful area. Since such an error level is still reasonable for an SNR of 50 dB, it can be concluded that the sparse recovery in the spherical NFFFT is sufficiently robust against measurement noise.

H. Influence of Probe Correction

To investigate a last possible influence on the transition bounds, the HD probe is replaced with a higher-order probe. Firstly, a 2-dimensional array of HDs as shown

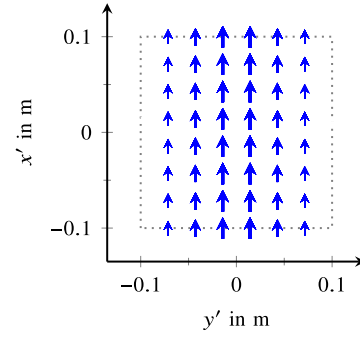


Fig. 10. HD array (6×8 in-phase HDs with an amplitude taper) used as a synthetic higher-order probe antenna.

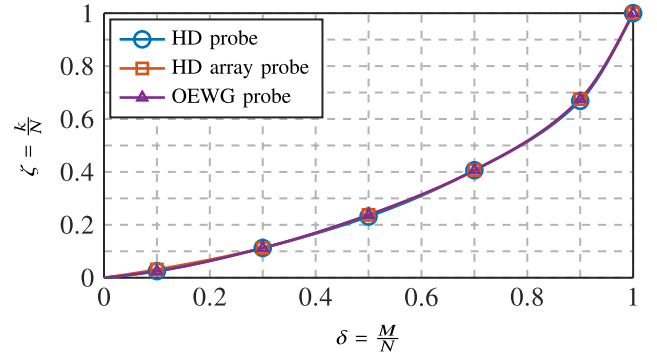


Fig. 11. Transition bounds corresponding to $N \leq -70$ dB for an HD array and an OEWG higher-order probe as well as a simple HD probe, all in the noiseless case and $\tau = 0$ using the BP recovery strategy.

in Fig. 10 is used as a probe [61]. From the analytical FF expression, the probe-receiving coefficients $R_{\sigma\mu\nu}^p$ [see (5)] are determined. Furthermore, the NSI-RF-WR284 open-ended waveguide (OEWG) [62] is used as a probe antenna.¹ Its probe-receiving coefficients are determined from the FF computed by FEKO [63]. The resulting transition bounds are shown in Fig. 11 together with the bound for the HD probe. As all three bounds are almost identical, it can be concluded that the previous results are also valid for the considered higher-order probes, at least for the noiseless case. As shown in the following, when measurement noise is present and BP_η is used, it appears that α needs to be increased.

I. Practically Relevant Case

After investigating the different influences on the recovery guarantees separately, the combination of sparsity defects and noise is of interest. To this end, a level of sparsity defects of $\tau = 2 \times 10^{-4}$ and noise levels of 60 dB, 50 dB, 40 dB, and 30 dB are simulated for an HD and the OEWG higher-order probe. The resulting PTDs (for the HD probe) and extracted bounds (for HD and OEWG probe) for different FF errors N are shown in Fig. 12. In general, the higher the requirements are on the error level, the more samples are required. As can be seen especially for the SNRs of 40 dB and 30 dB in Fig. 12, only for extremely low sparsity levels an error below

¹Note that OEOWGs are sometimes considered as first-order probes. However, this is only an approximation.

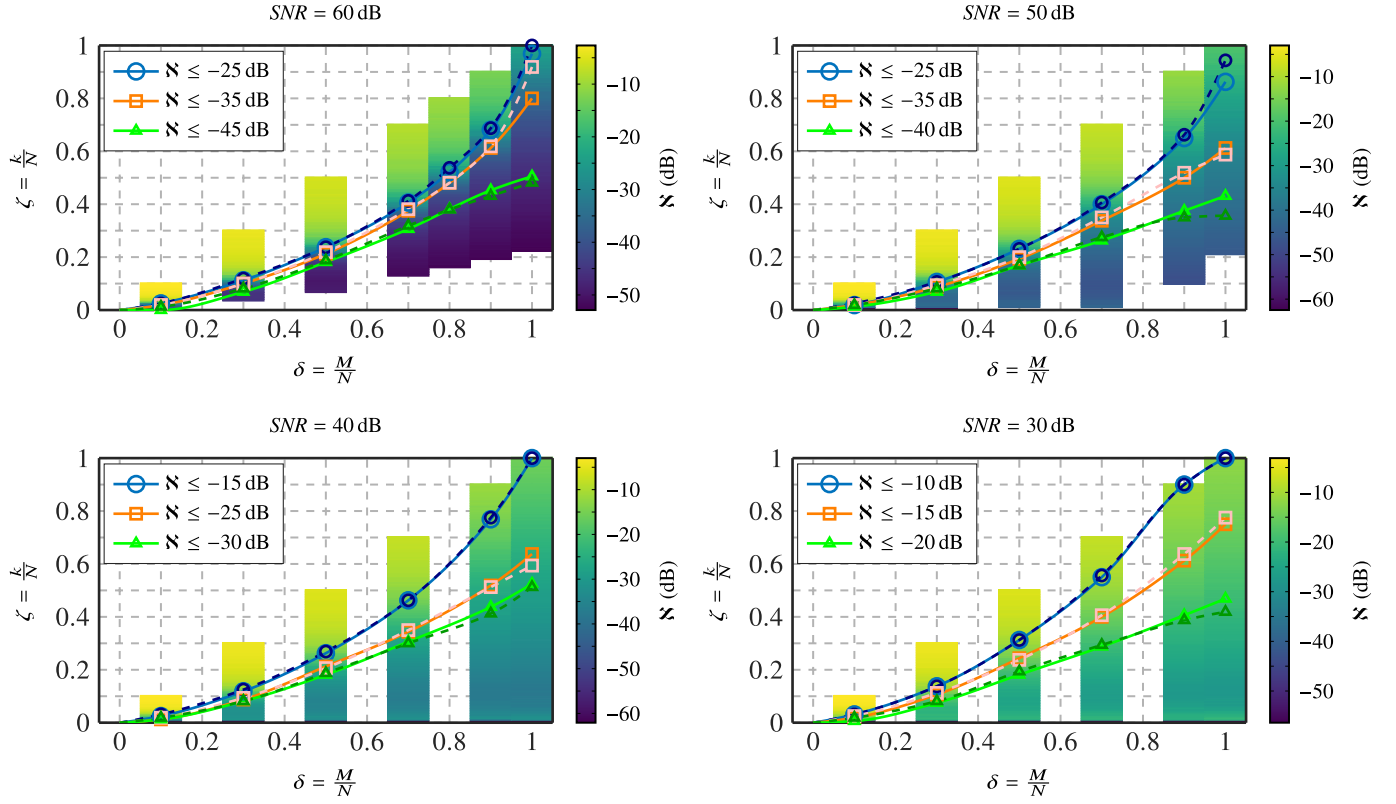


Fig. 12. PTDs for an HD probe and transition bounds for the HD probe and the OEWG higher-order probe (dashed). All for a level of sparsity defects of $\tau = 2 \times 10^{-4}$. As recovery strategy, the BP_η is used with $\eta = \alpha\sqrt{M}$, where $\alpha = 1.975 \times 10^{-5}$, 6.24×10^{-5} , 1.975×10^{-4} , and 6.24×10^{-4} for the HD probe and $\alpha = 5.139 \times 10^{-5}$, 1.925×10^{-4} , 5.639×10^{-4} , and 3.125×10^{-3} for the OEWG probe for an $\text{SNR} = 60, 50, 40$, and 30 dB, respectively.

the SNR can be achieved. Furthermore, for all noise levels, the transition bound slightly depends on the probe. Particularly, α has to be increased (using an empirical value) compared to the case using the HD probe. An explanation for this might be that a larger probe collects more noise. However, the determined bounds are still close to the ones using the HD probe, both lying in a useful range for NFFFTs based on simulation or measurement data of antennas.

In consequence, a practical approach could be to first of all determine the sparsity level of the spherical expansion coefficients of an AUT, for example, via simulation. Then, the PTD with the fitting SNR , τ , probe, and sampling grid can be used (if not available, it can be set up according to Section IV-A) to deduce the minimum number of samples in order to achieve the desired error level.

V. NFFFT RESULTS USING CS

In order to verify that the determined transition bounds hold for actual antennas, NFFFTs are performed with the number of sampling points predicted by the determined PTDs.

A. Simulation of a Horn Antenna

As a first example, a pyramidal horn antenna is considered. The NF data of the antenna are computed by FEKO, which determines a method of moments (MoM) solution. Based on a rectangular WR90 waveguide as feeding structure, the antenna geometry is defined as shown in Fig. 13. Excited is only

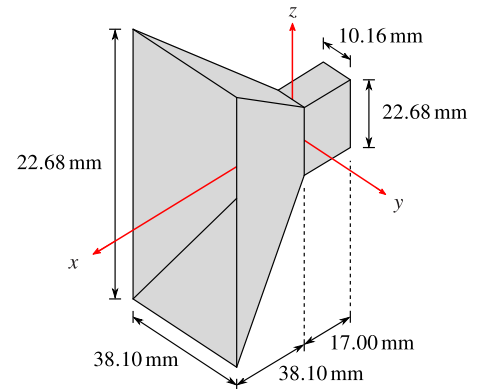


Fig. 13. Geometry of the simulated pyramidal horn antenna. The walls are perfectly electrically conducting (PEC) and infinitely thin.

the fundamental (TE_{10}) mode at a frequency of 11 GHz. The diameter of the minimum sphere of the antenna is $D = 124 \text{ mm} \approx 4.6\lambda$. With an $\epsilon = 11$, the number of spherical modes is determined from (3) as $L = 26$, which leads to $N = 1456$ expansion coefficients. The sampling points are again placed on a spiral grid as defined in (12)–(14) with a fixed radius of 0.1 m. The magnitude of the spectrum of the expansion coefficients x_{smn} is shown in Fig. 14 (can be directly determined by FEKO). While there is no actual zero entry, only 29% of the coefficients are larger in magnitude than 0.02% of the largest coefficient, that is, for $\tau = 2 \times 10^{-4}$,

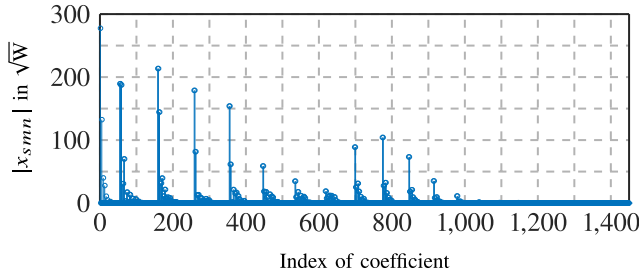


Fig. 14. Magnitude of the expansion coefficients of the simulated pyramidal horn antenna shown in Fig. 13.

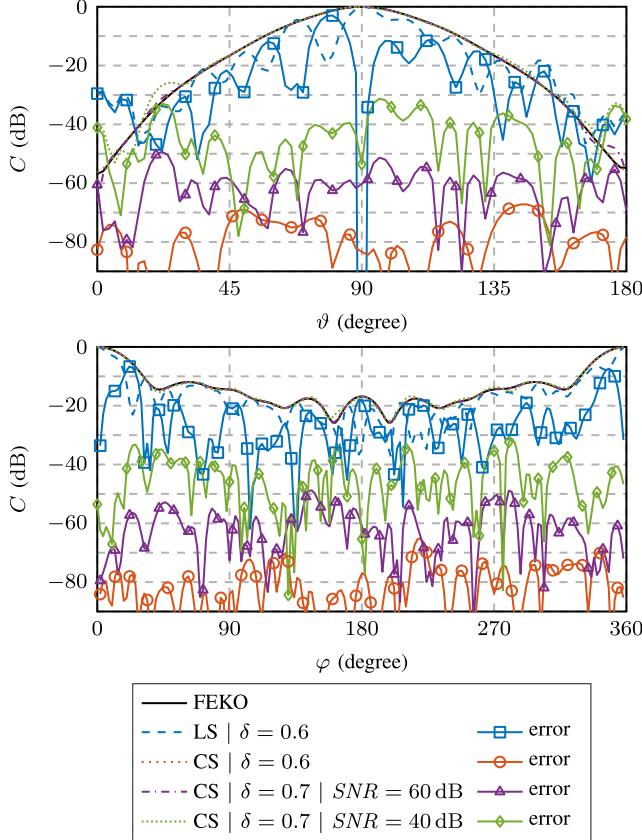


Fig. 15. Comparison of the reconstructed radiation characteristic C of the pyramidal horn antenna with the one from FEKO. The CS solutions use the BP in the noiseless case and BP_η with $\eta = \alpha\sqrt{M}$ in the noisy cases. Top: H-plane ($\varphi = 0$). Bottom: E-plane ($\vartheta = \pi/2$).

the sparsity level is $\zeta \approx 0.29$. Consequently, for an error of $\aleph \leq 60$ dB, it follows from Fig. 7 that $\delta \geq 0.6$ has to hold. This corresponds to a minimum amount of samples of $M = 874$.

An H-plane and an E-plane cut of the reconstructed FF by the BP is shown in Fig. 15 together with a regularized LS solution using the same measurement. The regularization is achieved by solving the normal equation system $\mathbf{A}^H \mathbf{y} = \mathbf{A}^H \mathbf{A} \mathbf{x}$ associated with (6) with the iterative generalized minimum residual method (GMRES) [64], which stops at a relative residual of 1×10^{-7} . Both the results are compared to the FF computed by FEKO. While the CS solution achieves the predicted FF error, the regularized LS solution shows

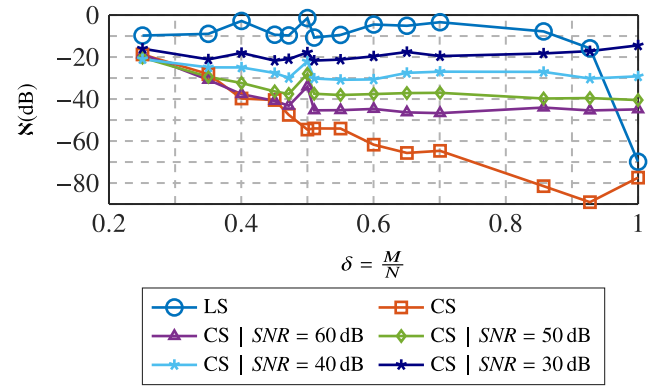


Fig. 16. Achieved error \aleph for the pyramidal horn antenna for different number of samples M using CS with BP and the regularized LS solution in the noiseless case, and CS with the BP_η in the noisy cases.

only a coarse resemblance with the correct antenna pattern (be reminded that only one polarization per sample is used).

Also shown in Fig. 15 are the reconstructed patterns for the case when noise with an SNR of 60 dB and 40 dB is added to the measurements. With a reconstruction error of $\aleph \leq -45$ dB and $\aleph \leq -30$ dB, the predictions of the (HD) transition bounds given in Fig. 12 are shown to hold. The bounds require at least $M = 0.7 N \approx 1020$ sampling points in order to achieve the corresponding error levels.

The error level for different number of samples is depicted in Fig. 16. In the noiseless case, for $\delta < 0.6$, the predicted $\aleph \leq -60$ dB from Fig. 7 can no longer be achieved by CS; however, above $\delta = 0.6$, even better error levels can be reached. In contrast, the regularized LS solution only leads to an acceptable accuracy for $\delta = 1.0$. For the noisy cases, the predictions of the PTDs in Fig. 12 hold true, as well. Interestingly, for $\delta < 0.6$, the encountered errors are better than predicted by the PTDs in Fig. 12. Consequently, one could conclude that the determined bounds are too pessimistic. However, the bounds have to hold for all antennas and not only this specific one. Hence, in order to make to bound even closer to the absolute minimum of samples, presumably more information about the specific antenna would have to be included in some form.

B. Concerning the Absolute Minimum of Samples

As already indicated by the previous results, it should be noted that the presented approach does not necessarily determine the absolute minimum of samples for the spherical NFFFT. First, for certain configurations (antennas and sampling locations), CS might find a solution with the same error level from even less measurements. However, contrary to the predictions by the PTDs, there is no guarantee to achieve this error level. Also, the LS solution could work sufficiently well, but again there is no guarantee. Finally, there is no definite way to choose ϵ in (3) and consequently the number of modes L . Selecting, for example, for the simulated horn antenna $\epsilon = 0$, a full-rank LSE can be achieved with only $M = 510$ measurements. This would be less than the previously used $M = 874$ samples for CS. However, solving the corresponding LSE, only an error of -30 dB can

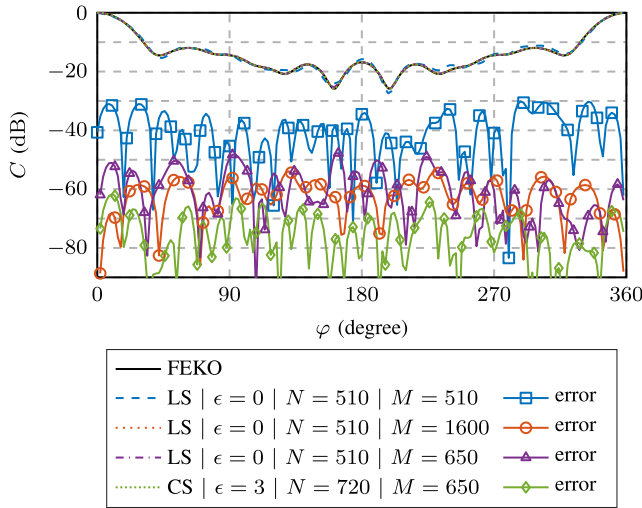


Fig. 17. Comparison of the E-plane of the reconstructed radiation characteristic C of the pyramidal horn antenna with the one from FEKO for different setups. The CS solution uses the BP.

be achieved as shown in Fig. 17. Increasing the number of samples to $M = 1600$ and taking two orthogonal polarizations improve the error to only about -55 dB, showing that the solution accuracy is limited due to the degrees of freedom of the model. In contrast, when choosing $\epsilon = 3$ ($N = 720$), a sparsity level of about 50% can be observed ($\tau = 2 \times 10^{-4}$). According to the PTD in Fig. 7, a CS reconstruction requires $N = 650$ samples. That the predicted error of about -60 dB is achieved can be seen from Fig. 17. The overdetermined solution for $\epsilon = 0$ using also $M = 650$ samples achieves only an error of -45 dB. Consequently, after choosing ϵ and L sufficiently large to represent the radiated fields of the AUT, the PTDs can predict the minimum amount of samples required for CS in order to achieve a certain error level.

C. Simulation of an Antenna Array

As a second example, a 21×23 rectangular Dolph-Chebyshev (in phase, amplitude tapered) array of z -directed HDs in the yz -plane is considered. At a frequency of 1 GHz, the distances and amplitudes are determined according to [65] and [66] such that a sidelobe level of -30 dB is achieved. With a minimum sphere diameter of $D = 27.9\lambda$ and $\epsilon = 11$, the order of the spherical mode expansion is $L = 99$ resulting in $N = 19998$ expansion coefficients. The spectrum of the expansion coefficients is determined by taking two orthogonal polarizations at 22 000 sample locations and obtaining the LS solution. Using $\tau = 2 \times 10^{-4}$, a sparsity level of $\zeta \approx 18\%$ is found. According to the transition bound in Fig. 7, $M = 0.49N \approx 9800$ samples should suffice to achieve an error of $\aleph \leq -60$ dB. The results shown in Fig. 18 verify this. When measurement noise with an SNR of 50 dB is added, it follows from Fig. 12 that $M = 0.55N \approx 10999$ and $M = 0.45N \approx 9000$ samples are required for an error of $\aleph \leq -40$ dB and $\aleph \leq -25$ dB, respectively. That both predictions hold true is verified in Fig. 12 as well.

The half power bandwidths $HPBW = 3.22^\circ$ in the E-plane and $HPBW = 2.91^\circ$ in the H-plane are reproduced in all

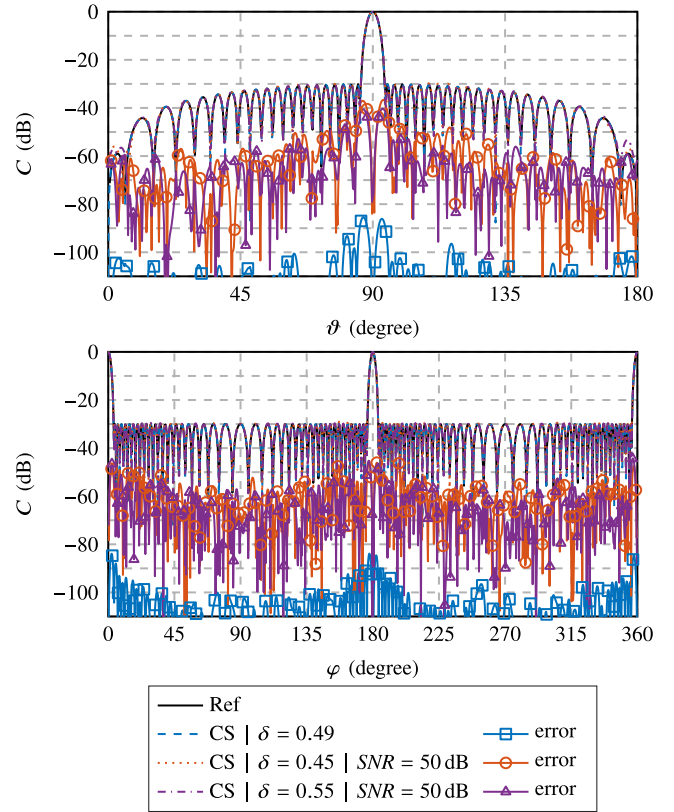


Fig. 18. Comparison of the reconstructed radiation characteristic C of the simulated Dolph-Chebyshev array with the analytical reference solution. The reconstruction by CS uses BP in the noiseless case and BP $_{\eta}$ in the noisy case. Top: E-plane ($\varphi = 0$). Bottom: H-plane ($\vartheta = \pi/2$).

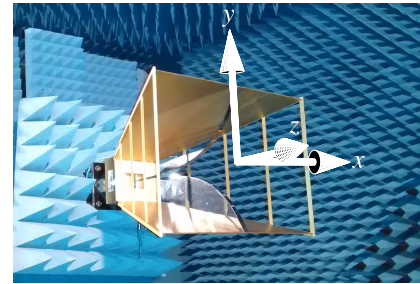


Fig. 19. Measured double-ridged DRH400 antenna from RFspin mounted in the anechoic chamber.

cases at least up to the third decimal place. The directivity $D_{\text{dir}} = 26.92$ dB is reproduced with a relative error of -156 dB, -18.12 dB, and -16.76 dB for the setups with $\delta = 0.49$ (noiseless), $\delta = 0.55$, and $\delta = 0.45$, respectively.

D. Measurement of a Double-Ridged Horn Antenna

Finally, the double-ridged DRH400 horn antenna [67] as shown in Fig. 19 is measured in an anechoic chamber at a frequency of 3 GHz with the NSI-RF-WR284 OEWG [62] as probe antenna. Initially, two orthogonal polarizations are obtained for $M = 16380$ samples on an equiangular grid. With a diameter of the minimum sphere of $D \approx 1.6 \text{ m} \approx 16\lambda$, the number of spherical modes is determined as $L = 79$, leading to $N = 12798$ expansion coefficients. The magnitude

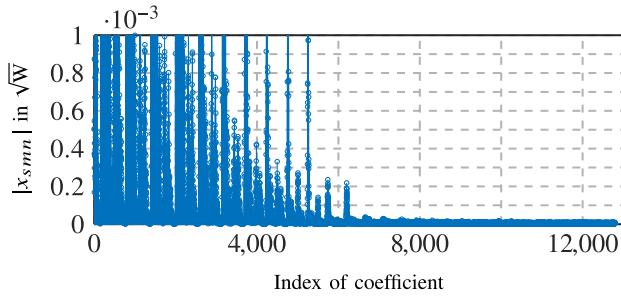


Fig. 20. Magnitude of the expansion coefficients of the measured double-ridged DRH400 antenna shown in Fig. 19. In order to visualize that none of the coefficients is zero, the large coefficients are cut off. The largest coefficient has a magnitude of $11 \times 10^{-2} \sqrt{W}$.

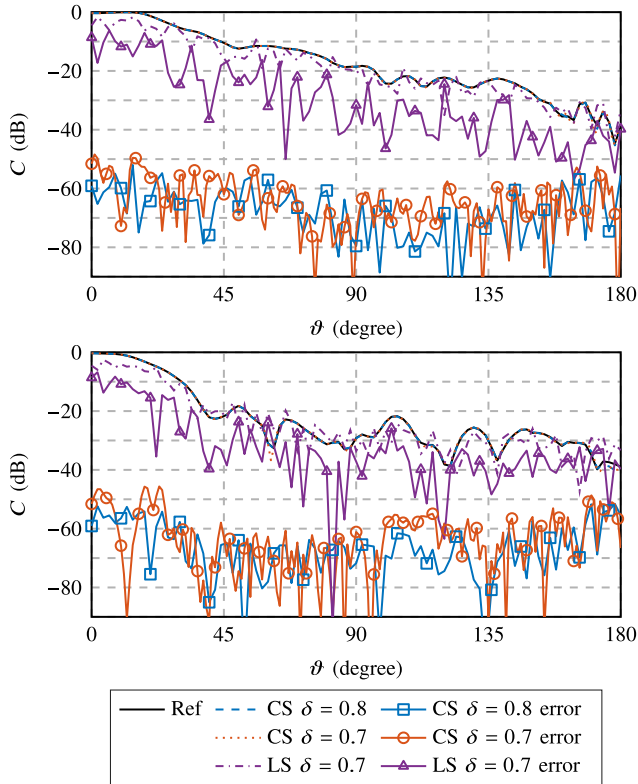


Fig. 21. Comparison of the reconstructed radiation characteristic C of the DRH400 antenna with a reference solution obtained by using two orthogonal polarizations for each of the $M = 16\,380$ sampling points. The reconstruction by CS uses for $\delta = 0.8$ corresponding to $M = 10\,239$ samples the BP_η ($\eta = 2.5 \times 10^{-3}$) and for $\delta = 0.7$ corresponding to $M = 8959$ samples the BP to reconstruct the $N = 12\,798$ expansion coefficients. The regularized LS solution uses also the $M = 8959$ samples. Top: H-plane ($\varphi = 0$). Bottom: E-plane ($\varphi = \pi/2$).

of the spectrum of the expansion coefficients is depicted in Fig. 20. The spectrum is determined by using both polarizations at all $M = 16\,380$ sampling points and solving the normal equation system $\mathbf{A}^H \mathbf{y} = \mathbf{A}^H \mathbf{A} \mathbf{x}$ associated with (6) with the iterative GMRES [64]. However, also a simulation of the antenna could be used. Using $\tau = 2 \times 10^{-4}$, a sparsity level of $\zeta \approx 0.33$ is determined. Since the SNR of the measurement is approximately 60 dB, it follows from the transition bound in Fig. 12 that at least $M = 0.7 N \approx 8959$ measurements are required in order to achieve an error level of $\aleph \leq -45$ dB.

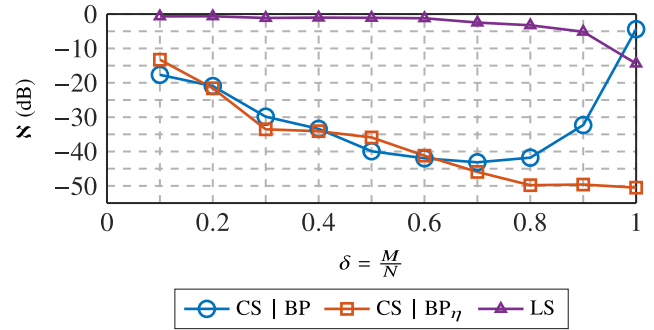


Fig. 22. Achieved error \aleph for the measured DRH400 antenna for different number of samples M using CS and the regularized LS solution.

In Fig. 21, the reconstructed FF in the H-plane and E-plane is depicted. For the reconstruction using CS, a spiral grid with the desired number of points is defined and the closest points of the equiangular grid are selected. For each selected point, one of the two polarizations is randomly chosen. The deviation of the CS solution (using the BP) to the reference solution (using the $M = 16\,380$ sampling points) is for $M = 8959$ ($\delta = 0.7$) for all angles below the predicted -45 dB. Again, the regularized LS solution shows only a rough resemblance with the reference. If the number of measurements is increased to $M = 10\,239$ ($\delta = 0.8$), the worst case deviation of CS decreases as expected to a level lower than -50 dB.

Investigating the error for different number of measurements M as shown in Fig. 22 verifies that BP_η achieves $\aleph \leq -45$ dB only for $\delta \geq 0.7$. Similar to the simulated horn antenna, the encountered error is for $\delta < 0.7$ better than predicted by the PTD in Fig. 12. Furthermore, the insights from Fig. 8 concerning the performance of BP in the noisy case are confirmed. From about $\delta \geq 0.7$ on (note that a different probe is used) the error increases again.

VI. CONCLUSION

It has been shown how to predict the minimum number of samples required for a CS reconstruction in the spherical NFFFT by using PTDs. The latter depend on the required error level in the FF. Consequently, CS can be applied to the spherical NFFFT in a reliable manner. This allows reducing the number of samples if prior knowledge about the sparsity of the spherical expansion coefficients can be obtained. The investigation of several influence factors showed that a deterministic spiral grid is well suited. Furthermore, measurement noise and sparsity defects increase the minimum number of measurements and decrease the achievable error level but within a range which is still useful for antenna NF measurements. For noisy measurements in combination with the quadratically constrained (BP_η), different probes require careful adjustment of the constraint.

For the considered antennas, the number of sampling points was reduced by up to 55%. Relaxing the requirements on the FF error can lead to a further reduction. Considering that only one polarization has to be measured at each sampling point and that most other approaches so far usually acquire more samples than there are unknowns (e.g., in order to average

out noise), the achieved reduction in sampling points is even higher.

The used approach with PTDs could also be adapted for other applications, where the possible influences can each be captured in one parameter.

REFERENCES

- [1] A. D. Yaghjian, "An overview of near-field antenna measurements," *IEEE Trans. Antennas Propag.*, vol. 34, no. 1, pp. 30–45, Jan. 1986.
- [2] J. L. A. Quijano and G. Vecchi, "Field and source equivalence in source reconstruction on 3D surfaces," *Progr. Electromagn. Res.*, vol. 103, pp. 67–100, 2010.
- [3] Y. Álvarez, F. Las-Heras, and M. R. Pino, "Reconstruction of equivalent currents distribution over arbitrary three-dimensional surfaces based on integral equation algorithms," *IEEE Trans. Antennas Propag.*, vol. 55, no. 12, pp. 3460–3468, Dec. 2007.
- [4] T. F. Eibert and C. H. Schmidt, "Multilevel fast multipole accelerated inverse equivalent current method employing Rao–Wilton–Glisson discretization of electric and magnetic surface currents," *IEEE Trans. Antennas Propag.*, vol. 57, no. 4, pp. 1178–1185, Apr. 2009.
- [5] T. F. Eibert, E. Kılıç, C. Lopez, R. A. Mauermayer, O. Neitz, and G. Schnattinger, "Electromagnetic field transformations for measurements and simulations (invited paper)," *Progr. Electromagn. Res.*, vol. 151, pp. 127–150, 2015.
- [6] M. A. Qureshi, C. H. Schmidt, and T. F. Eibert, "Efficient near-field far-field transformation for nonredundant sampling representation on arbitrary surfaces in near-field antenna measurements," *IEEE Trans. Antennas Propag.*, vol. 61, no. 4, pp. 2025–2033, Apr. 2013.
- [7] O. Neitz, R. A. M. Mauermayer, Y. Weitsch, and T. F. Eibert, "A propagating plane-wave-based near-field transmission equation for antenna gain determination from irregular measurement samples," *IEEE Trans. Antennas Propag.*, vol. 65, no. 8, pp. 4230–4238, Aug. 2017.
- [8] J. E. Hansen, Ed., *Spherical Near-Field Antenna Measurements*. Stevenage, U.K.: IET, 2008.
- [9] R. A. M. Mauermayer and T. F. Eibert, "Spherical field transformation above perfectly electrically conducting ground planes," *IEEE Trans. Antennas Propag.*, vol. 66, no. 3, pp. 1465–1478, Mar. 2018.
- [10] O. Bucci, C. Gennarelli, G. Riccio, and C. Savarese, "Fast and accurate far-field evaluation from a non redundant, finite number of plane polar measurements," in *Proc. IEEE Antennas Propag. Soc. Int. Symp. URSI Nat. Radio Sci. Meeting*, Seattle, WA, USA, Jun. 1994, pp. 540–543.
- [11] F. D'Agostino, F. Ferrara, C. Gennarelli, R. Guerriero, and M. Migliozi, "Fast and accurate far-field prediction by using a reduced number of bipolar measurements," *IEEE Antennas Wireless Propag. Lett.*, vol. 16, pp. 2939–2942, 2017.
- [12] P.-J. Chiu, D.-C. Tsai, and Z.-M. Tsai, "Fast near-field antenna measurement technique," in *Proc. Eur. Microw. Conf. (EuMC)*, Paris, France, Sep. 2015, pp. 594–597.
- [13] S. C. Kordella and K. R. Grimm, "Determination of the far-field radiation pattern of an antenna from a set of sparse near-field measurements," in *Proc. AMTA*, Austin, TX, USA, Oct./Nov. 2016, pp. 1–6.
- [14] R. A. M. Mauermayer and T. F. Eibert, "Combining the fast irregular antenna field transformation algorithm with asymptotic high frequency methods," in *Proc. EuCAP*, Piscataway, NJ, USA, Apr. 2015, pp. 1–4.
- [15] E. J. Candès, J. Romberg, and T. Tao, "Robust uncertainty principles: Exact signal reconstruction from highly incomplete frequency information," *IEEE Trans. Inf. Theory*, vol. 52, no. 2, pp. 489–509, Feb. 2006.
- [16] D. L. Donoho, "Compressed sensing," *IEEE Trans. Inf. Theory*, vol. 52, no. 4, pp. 1289–1306, Apr. 2006.
- [17] E. J. Candès and T. Tao, "Near-optimal signal recovery from random projections: Universal encoding strategies?" *IEEE Trans. Inf. Theory*, vol. 52, no. 12, pp. 5406–5425, Dec. 2006.
- [18] T. Strohmer, "Measure what should be measured: Progress and challenges in compressive sensing," *IEEE Signal Process. Lett.*, vol. 19, no. 12, pp. 887–893, Dec. 2012.
- [19] M. Elad, "Sparse and redundant representation modeling—What next?" *IEEE Signal Process. Lett.*, vol. 19, no. 12, pp. 922–928, Dec. 2012.
- [20] A. Massa, P. Rocca, and G. Oliveri, "Compressive sensing in electromagnetics—A review," *IEEE Antennas Propag. Mag.*, vol. 57, no. 1, pp. 224–238, Feb. 2015.
- [21] J. Ender, "A brief review of compressive sensing applied to radar," in *Proc. 14th Int. Radar Symp. (IRS)*, Dresden, Germany, Jun. 2013, pp. 3–16.
- [22] M. D. Migliore, "A simple introduction to compressed sensing/sparse recovery with applications in antenna measurements," *IEEE Antennas Propag. Mag.*, vol. 56, no. 2, pp. 14–26, Apr. 2014.
- [23] M. D. Migliore, "On the sampling of the electromagnetic field radiated by sparse sources," *IEEE Trans. Antennas Propag.*, vol. 63, no. 2, pp. 553–564, Feb. 2015.
- [24] B. Fuchs, L. Le Coq, S. Rondineau, and M. D. Migliore, "Fast antenna far-field characterization via sparse spherical harmonic expansion," *IEEE Trans. Antennas Propag.*, vol. 65, no. 10, pp. 5503–5510, Oct. 2017.
- [25] P. Abrial, Y. Moudden, J.-L. Starck, J. Fadili, J. Delabrouille, and M. Nguyen, "CMB data analysis and sparsity," *Statist. Methodol.*, vol. 5, no. 4, pp. 289–298, Jul. 2008.
- [26] H. Rauhut and R. Ward, "Sparse recovery for spherical harmonic expansions," Feb. 2011, *arXiv:1102.4097v1*. [Online]. Available: <https://arxiv.org/abs/1102.4097v1>
- [27] N. Burg, S. Dyatlov, R. Ward, and M. Zworski, "Weighted eigenfunction estimates with applications to compressed sensing," *SIAM J. Math. Anal.*, vol. 44, no. 5, pp. 3481–3501, Jan. 2012.
- [28] Y. F. Alem, D. H. Chae, and S. M. A. Salehin, "Sparse recovery on sphere via probabilistic compressed sensing," in *Proc. IEEE Workshop Stat. Signal Process. (SSP)*, Gold Coast, VIC, Australia, Jun./Jul. 2014, pp. 380–383.
- [29] Y. F. Alem, S. M. A. Salehin, D. H. Chae, and R. A. Kennedy, "Sparse recovery of spherical harmonic expansions from uniform distribution on sphere," in *Proc. 7th Int. Conf. Signal Process. Commun. Syst. (ICSPCS)*, Carrara, VIC, Australia, Dec. 2013, pp. 1–5.
- [30] R. Cornelius, D. Heberling, N. Koep, A. Behboodi, and R. Mathar, "Compressed sensing applied to spherical near-field to far-field transformation," in *Proc. 10th Eur. Conf. Antennas Propag. (EuCAP)*, Davos, Switzerland, Apr. 2016, pp. 1–4.
- [31] D. Löschenbrand and C. Mecklenbrauker, "Fast antenna characterization via a sparse spherical multipole expansion," in *Proc. 4th Int. Workshop Compress. Sens. Theory Appl. Radar, Sonar Remote Sens. (CoSeRa)*, Aachen, Germany, Sep. 2016, pp. 212–216.
- [32] A. Bangun, A. Behboodi, and R. Mathar, "Sparse recovery in Wigner-D basis expansion," in *Proc. IEEE Global Conf. Signal Inf. Process. (GlobalSIP)*, Washington, DC, USA, Dec. 2016, pp. 287–291.
- [33] D. L. Donoho and J. Tanner, "Precise undersampling theorems," *Proc. IEEE*, vol. 98, no. 6, pp. 913–924, Jun. 2010.
- [34] D. Donoho and J. Tanner, "Observed universality of phase transitions in high-dimensional geometry, with implications for modern data analysis and signal processing," *Philos. Trans. Roy. Soc. A, Math., Phys. Eng. Sci.*, vol. 367, no. 1906, pp. 4273–4293, Nov. 2009.
- [35] B. Hofmann and T. F. Eibert, "Sparse recovery with predictable accuracy in noisy spherical antenna near-field measurements," in *Proc. IEEE Int. Symp. Antennas Propag. (APS)*, Atlanta, GA, USA, Jul. 2019, pp. 1–2.
- [36] S. Foucart and H. Rauhut, *A Mathematical Introduction to Compressive Sensing (Applied and Numerical Harmonic Analysis)*. New York, NY, USA: Springer, 2013.
- [37] M. F. Duarte and Y. C. Eldar, "Structured compressed sensing: From theory to applications," *IEEE Trans. Signal Process.*, vol. 59, no. 9, pp. 4053–4085, Sep. 2011.
- [38] Y. C. Eldar and G. Kutyniok, Eds., *Compressed Sensing: Theory and Applications*. Cambridge, U.K.: Cambridge Univ. Press, 2012.
- [39] D. L. Donoho and X. Huo, "Uncertainty principles and ideal atomic decomposition," *IEEE Trans. Inf. Theory*, vol. 47, no. 7, pp. 2845–2862, Nov. 2001.
- [40] J. A. Tropp, "Greed is good: Algorithmic results for sparse approximation," *IEEE Trans. Inf. Theory*, vol. 50, no. 10, pp. 2231–2242, Oct. 2004.
- [41] E. J. Candès and T. Tao, "Decoding by linear programming," *IEEE Trans. Inf. Theory*, vol. 51, no. 12, pp. 4203–4215, Dec. 2005.
- [42] A. M. Tillmann and M. E. Pfetsch, "The computational complexity of the restricted isometry property, the nullspace property, and related concepts in compressed sensing," *IEEE Trans. Inf. Theory*, vol. 60, no. 2, pp. 1248–1259, Feb. 2014.
- [43] J. D. Blanchard, C. Cartis, and J. Tanner, "Compressed sensing: How sharp is the restricted isometry property?" *SIAM Rev.*, vol. 53, no. 1, pp. 105–125, Jan. 2011.
- [44] M. Fornasier, Ed., *Theoretical Foundations and Numerical Methods for Sparse Recovery* (Radon Series on Computational and Applied Mathematics). Berlin, Germany: De Gruyter, 2010.
- [45] D. L. Donoho, "High-dimensional centrally symmetric polytopes with neighborliness proportional to dimension," *Discrete Comput. Geometry*, vol. 35, no. 4, pp. 617–652, May 2006.

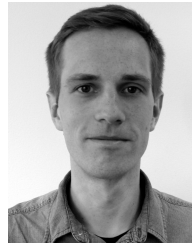
- [46] D. L. Donoho and J. Tanner, "Neighborliness of randomly projected simplices in high dimensions," *Proc. Nat. Acad. Sci.*, vol. 102, no. 27, pp. 9452–9457, Jul. 2005.
- [47] D. L. Donoho and J. Tanner, "Counting faces of randomly projected polytopes when the projection radically lowers dimension," *J. Amer. Math. Soc.*, vol. 22, no. 1, pp. 1–53, Jul. 2008.
- [48] D. L. Donoho and J. Tanner, "Exponential bounds implying construction of compressed sensing matrices, error-correcting codes, and neighborly polytopes by random sampling," *IEEE Trans. Inf. Theory*, vol. 56, no. 4, pp. 2002–2016, Apr. 2010.
- [49] W. Xu and B. Hassibi, "Precise stability phase transitions for ℓ_1 minimization: A unified geometric framework," *IEEE Trans. Inf. Theory*, vol. 57, no. 10, pp. 6894–6919, Oct. 2011.
- [50] Y. Zhang, "Theory of compressive sensing via ℓ_1 -minimization: A non-RIP analysis and extensions," *J. Oper. Res. Soc. China*, vol. 1, no. 1, pp. 79–105, Mar. 2013.
- [51] M. Stojnic, W. Xu, and B. Hassibi, "Compressed sensing—Probabilistic analysis of a null-space characterization," in *Proc. IEEE Int. Conf. Acoust. Speech Signal Process.*, Las Vegas, NV, USA, Mar./Apr. 2008, pp. 3377–3380.
- [52] M. Stojnic, W. Xu, and B. Hassibi, "Compressed sensing of approximately sparse signals," in *Proc. IEEE Int. Symp. Inf. Theory*, Toronto, ON, Canada, Jul. 2008, pp. 2182–2186.
- [53] M. Stojnic, " ℓ_1 optimization and its various thresholds in compressed sensing," in *Proc. IEEE Int. Conf. Acoust., Speech Signal Process.*, Dallas, TX, USA, Mar. 2010, pp. 3910–3913.
- [54] M. Grant and S. Boyd. (Mar. 2014). *CVX: MATLAB Software for Disciplined Convex Programming, Version 2.1*. [Online]. Available: <http://cvxr.com/cvx>
- [55] M. C. Grant and S. P. Boyd, "Graph implementations for nonsmooth convex programs," in *Recent Advances in Learning and Control* (Lecture Notes in Control and Information Sciences), V. D. Blondel, S. P. Boyd, and H. Kimura, Eds. London, U.K.: Springer-Verlag, 2008, pp. 95–110.
- [56] MOSEK. (2015). Version 7.1.0.12. MOSEK ApS, Copenhagen, Denmark, [Online]. Available: <http://www.mosek.com>
- [57] E. van den Berg and M. P. Friedlander, "Probing the Pareto frontier for basis pursuit solutions," *SIAM J. Sci. Comput.*, vol. 31, no. 2, pp. 890–912, Jan. 2009.
- [58] J. Tanner. (Apr. 2012). *Phase Transitions of the Regular Polytopes and Cone*. [Online]. Available: <https://people.maths.ox.ac.uk/tanner/polytopes.shtml>
- [59] E. B. Saff and A. B. J. Kuijlaars, "Distributing many points on a sphere," *Math. Intell.*, vol. 19, no. 1, pp. 5–11, 1997.
- [60] S. Brugiapaglia and B. Adcock, "Robustness to unknown error in sparse regularization," *IEEE Trans. Inf. Theory*, vol. 64, no. 10, pp. 6638–6661, Jan. 2018.
- [61] C. H. Schmidt, D. T. Schobert, and T. F. Eibert, "Electric dipole based synthetic data generation for probe-corrected near-field antenna measurements," in *Proc. 5th Eur. Conf. Antennas Propag. (EUCAP)*, Rome, Italy, Apr. 2011, pp. 3269–3273.
- [62] NSI-MI. (Nov. 2018). *Model NSI-RF-Wr284 Open Ended Waveguide*. [Online]. Available: <https://www.nsi-mi.com>
- [63] FEKO, document Version 14.0-273612 (x64). Altair Engineering, Troy, MI, USA. 2017.
- [64] Y. Saad, *Iterative Methods for Sparse Linear Systems*, 2nd ed. Philadelphia, PA, USA: Society for Industrial and Applied Mathematics, 2003.
- [65] C. L. Dolph, "A current distribution for broadside arrays which optimizes the relationship between beam width and side-lobe level," *Proc. IRE*, vol. 34, no. 6, pp. 335–348, Jun. 1946.
- [66] A. Safaai-Jazi, "A new formulation for the design of Chebyshev arrays," *IEEE Trans. Antennas Propag.*, vol. 42, no. 3, pp. 439–443, Mar. 1994.
- [67] RFspin. (Dec. 2017). *Model DRH400 Double Ridged Waveguide Horn*. [Online]. Available: <http://www.rfspin.cz>



Bernd Hofmann (S'17) received the B.Eng. degree in electrical engineering from the Augsburg University of Applied Sciences, Augsburg, Germany, in 2015 and the M.Sc. degree in electrical engineering and information technology from the Technical University of Munich (TUM), Munich, Germany, in 2017.

Since 2017, he has been a Research Assistant with the Chair of High-Frequency Engineering, Department of Electrical and Computer Engineering, TUM. His current research interests include computational

electromagnetics, compressed sensing, and antenna near-field measurement techniques.



Ole Neitz (S'15) received the Dipl.-Ing. degree in electrical engineering and information technology from the University of Bremen, Bremen, Germany, in 2013.

From 2013 to 2019, he was a Research Assistant with the Chair of High-Frequency Engineering, Department of Electrical and Computer Engineering, Technical University of Munich, Munich, Germany. In 2019, he joined the Antenna Development Department, Rohde & Schwarz GmbH & Company KG., Munich. His current research

interests include antenna development and measurement techniques, near-field scattering, and imaging problems.



Thomas F. Eibert (S'93–M'97–SM'09) received the Dipl.-Ing. (FH) degree from Fachhochschule Nürnberg, Nuremberg, Germany, in 1989, the Dipl.-Ing. degree from Ruhr-Universität Bochum, Bochum, Germany, in 1992, and the Dr.-Ing. degree from Bergische Universität Wuppertal, Wuppertal, Germany, in 1997, all in electrical engineering.

He is currently a Full Professor of high-frequency engineering with the Technical University of Munich, Munich, Germany.